Antiproliferative properties of iron supramolecular cylinders

Rosa F. Brissos [a], Luís Korrodi-Gregório [b], Ricardo Pérez-Tomás [b], Olivier Roubeau [c], Patrick Gamez [a,d,e*]

Email: patrick.gamez@qi.ub.es

[a] Department of Inorganic and Organic Chemistry, Inorganic Chemistry Section, University of Barcelona, Martí i Franquès 1-11, 08028 Barcelona, Spain.
[b] Department of Pathology and Experimental Therapeutics, Faculty of Medicine, University of Barcelona, Campus Bellvitge, Feixa Llarga s/n, 08907 L'Hospitalet de Llobregat, Spain.
[c] Instituto de Ciencia de Materiales de Aragón, CSIC and Universidad de Zaragoza, Plaza San Francisco s/n, 50009 Zaragoza, Spain.
[d] Catalan Institution for Research and Advanced Studies, Passeig Lluís Companys 23, 08010 Barcelona, Spain.
[e] Institute of Nanoscience and Nanotechnology (IN2UB), Martí i Franquès 1-11, 08028 Barcelona, Spain.

Abstract: The use of metallohelicates as potential antiproliferative agents is mostly exemplified by one sole family of supramolecular compounds that is based on bis-iminopyridine ligands. In the present investigation, two other types of metallocylinders have been selected and their potential DNA-binding and cytotoxic properties have been investigated. Hence, two new neutral iron(III) metallosupramolecular compounds have been prepared from bis-β-diketone ligands, and a known cationic iron(II) helicate from bis-pyrazole ligands has been used for comparison purposes. DNA-interaction experiments and cell studies reveal remarkable biological properties for one of the neutral iron cylinders and the positively charged, pyrazole-based helicate, as illustrated by their antiproliferative behaviours, which are far better than those of two well-known compounds, *i.e.* the most studied metallohelicate in the field and cisplatin.

Keywords: DNA binding, metallohelicates, supramolecular interactions, cytotoxicity, iron metallocylinders, β-diketones, cell cycle, apoptosis.

I. Introduction

Cancer represents a major global health concern; for instance, it was responsible for 8.9 million deaths in 2015 [1]. Nearly 17% of worldwide deaths are due to cancer [2].
Chemotherapy is the use of (chemical) drugs designed to impede or slow the growth and reproduction of rapidly dividing cancer cells. Interest in metal-containing anticancer drugs began with the discovery of the cytotoxic properties of cisplatin in the 1960s [3]. Since 1978, cisplatin is broadly used clinically although it produces unpleasant side effects [4]. Furthermore, some tumours may display intrinsic or acquired resistance toward this inorganic compound [5]. Therefore, the development of new and more efficient drugs is important; as a matter of fact, a second- and third-generation of platinum drugs were developed [6,7]. However, they could only alleviate some of the drawbacks of the original platinum complex. In fact, many of the problems encountered with cisplatin are observed with newly designed coordination compounds (*i.e.*, of platinum or other metal ions), and thus remain unsolved [3]. Hence, new strategies are necessary to develop more selective and effective, metal-based anticancer agents (with distinct mechanism(s) of action).

DNA is a common target in the field of anticancer drug discovery [8]. Actually, this biomolecule is the main target of cisplatin, to which it strongly binds [9]. Obviously, any perturbation of DNA function may affect crucial cellular events like the transcription (*i.e.* gene expression and protein synthesis) or the replication, ultimately resulting in cell death [10]. Consequently, the design of molecules aiming at disturbing DNA's biological activity has been explored extensively [11-13].
DNA-protein recognition processes typically take place in the major groove of the double helix, through supramolecular contacts; these interactions usually occur with specific protein-surface motifs like helix-turn-helix motifs, zinc fingers, zipper motifs, β sheets or β hairpins [14,15]. In that context, supramolecular helices may mimic such protein frameworks and bind in the major groove of DNA, hence blocking cellular activities. It has been reported that some metallohelicates can act as α-helix protein motifs that recognize the major groove [16-19]; some of such supramolecular metal-containing helicates have shown interesting pro-apoptotic properties [20].
Non-covalent interactions of guest molecules (*e.g.* proteins) in the major groove rely on the establishment of specific hydrogen-bonding contacts with the host [21]. Accordingly, synthetic compounds aimed at binding in the major groove should be rationally designed; they should have the appropriate size to perfectly fit in the major groove but should also be large enough to avoid their interaction in the minor groove. In this respect, metallo-supramolecular cylinders such as metallohelicates show great potential [22-27]; however, their use in drug design is minimal [28], probably due to synthetic issues, their preparation often being more intricate than that of the (mono)metallic complexes normally used in the field.
So far, metallo-supramolecular cylinders designed to interact with DNA (and RNA) *via* non-covalent bonds, have been obtained from nitrogen-containing ligands [29-32]. In the present study, two new triple-stranded, iron(III) metallocylinders were prepared from oxygen-containing, dinucleating ligands, namely bis-β-diketones [33]. Their *in vitro* DNA-interacting and biological/cytotoxic properties were subsequently investigated, and compared with those of two known nitrogen-based iron helicates, *viz.* $[Fe_2(C_{25}H_{20}N_4)_3]Cl_4$ (**R1**) [17] and $Cl@[Fe_2(C_{22}H_{16}N_6)_3]Cl(PF_6)_2$ (**R2**) [34], which are depicted in **Figure S1**.

II. Results and Discussion

Synthesis

Bis-β-diketones can easily be synthesized in good yields by Claisen condensation between for instance a diester and two ketones [33], as depicted in **Scheme 1A** (see Materials and Methods section for details).

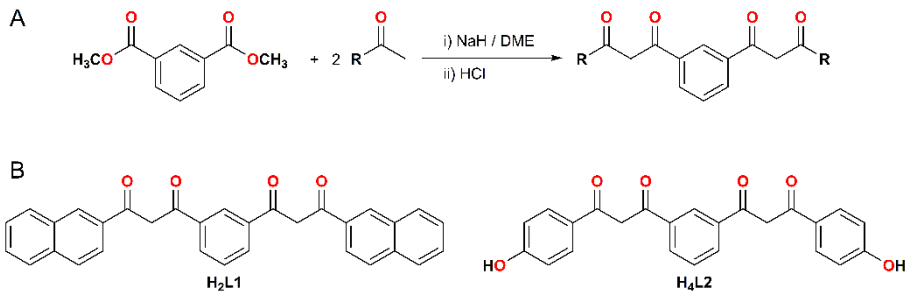

Scheme 1. A) Typical Claisen condensation reaction used to prepare bis-β-diketone ligands. B) 1,3-Bis-(3-oxo-3-(2-naphthyl)-propionyl)benzene (**H_2L1**) and 1,3-bis-(3-oxo-3-(4-hydroxyphenyl)propionyl)benzene (**H_4L2**).

Two β-diketone ligands were prepared, which contained distinct supramolecular-bond promoters, namely naphthyl groups (**H_2L1**) or phenol moieties (**H_4L2**) (Scheme 1B). These functional groups can indeed favour their interaction with DNA, *via* π−π stacking between base pairs (naphthyl groups, **H_2L1**) or hydrogen bonding with nitrogenous bases or/and phosphate-sugar backbone (phenol groups, **H_4L2**).

Two metallo-supramolecular cylinders were subsequently synthesized; hence, reaction of three equivalents of ligand with two equivalents of iron(III) chloride in the presence of a base (*i.e.* $NaHCO_3$), produced the corresponding (and expected) neutral, triple-stranded supramolecular complexes, as dark-red compounds (see Materials and Methods section for details). Indeed, comparable iron(III) helicates, which were prepared for their potentially interesting magnetic properties, have been reported in the literature [35]. Crystals of $[Fe(\mathbf{L1})_3](MeCN)(THF)_{0.25}$ (**H1**) and $[Fe(\mathbf{H_2L2})_3](MeCN)_2(H_2O)_2$ (**H2**), suitable for X-ray diffraction studies, could be obtained (see Experimental section).

Solid-state Structures

Compound **H1** crystallizes in the centrosymmetric triclinic space group *P*−1 (**Table S1**). Selected bond distances and angles are given in **Table S2**. **H1** contains two iron(III) ions that are wrapped by three deprotonated $\mathbf{L1}^{2-}$ ligands, generating a neutral, triple-stranded helicate with Δ−Δ or Λ−Λ metal configuration sets, both present in the crystal lattice.

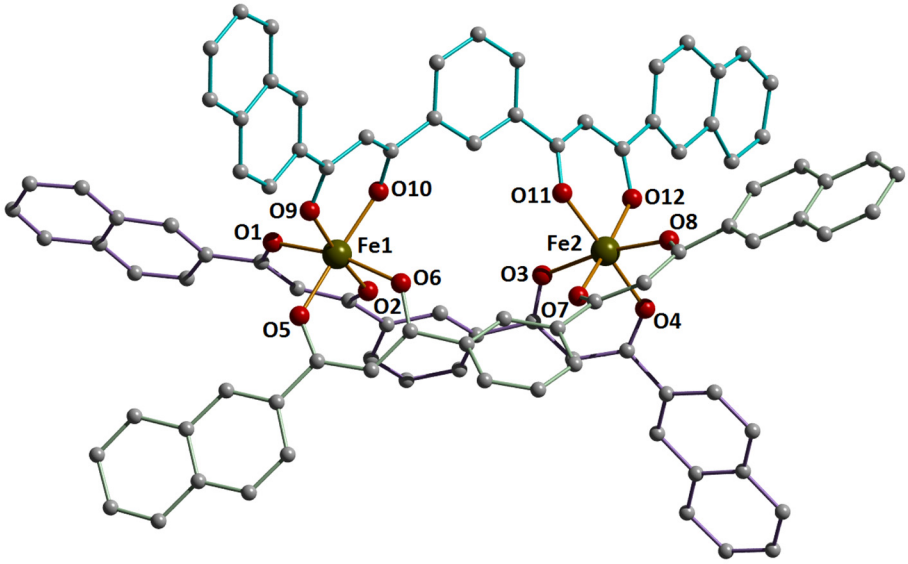

Figure 1. Representation of the crystal structure of **H1**. Hydrogen atoms and lattice solvent molecules are omitted for clarity. The three $\mathbf{L1}^{2-}$ ligands are shown with different colours.

The metal centres are in a slightly distorted octahedral O6 environment (the O−Fe−O angles varying from 83.60(18) to 97.48(18)° for Fe1, and 86.95(17) to 97.1(2)° for Fe2; see **Table S2**), generated by three β-diketonate moieties. The Fe−O bond distances are in normal ranges for such chromophore; for instance, they are like those observed for $Fe(acac)_3$ [36]. The crystal packing of **H1** reveals that the naphthyl groups of the ligands are, as anticipated (since the ligand $\mathbf{H_2L1}$ was designed for this purpose), involved in the formation of an intricate supramolecular 3D network assembled through π−π interactions (**Figure 2**). The strongest $\pi_{naphthyl}$−$\pi_{naphthyl}$ contact is illustrated in **Figure 2**, where the shortest carbon−carbon distance amounts to 3.383(18) Å, and the centroid-to-centroid distance is 3.712(2) Å (see **Table S3**). It can finally be pointed out that **H1** exists in two conformations in the lattice (in a 60:40 ratio), which are shown in **Figure S2**. These two conformations differ by the respective positions of two naphthyl moieties, displayed in pink and blue in **Figure S2**. Actually, it appears that the different orientations of these naphthyl groups are determined by the occurrence of distinct π−π interactions with neighbouring naphthyls (from adjacent helicates) in the lattice.

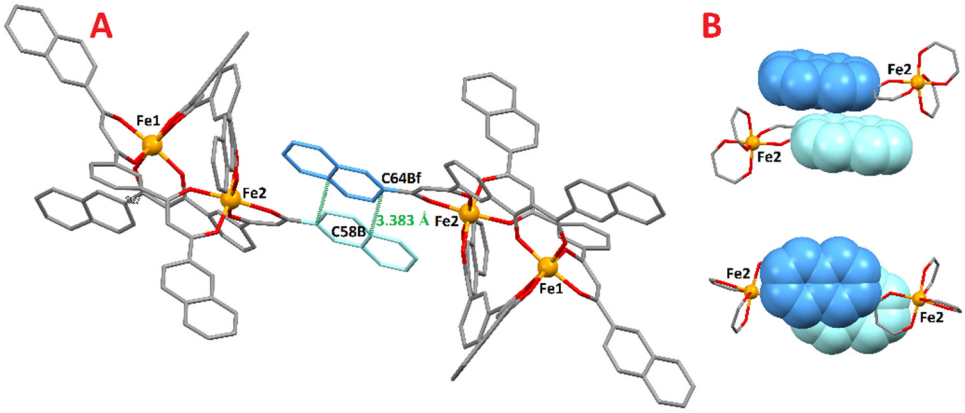

Figure 2. Example of strong π−π interactions between adjacent naphthyl groups observed in the crystal packing of **H1**. A) Strong contact between two **H1** molecules; C58B···C64Bf = 3.383(18) Å. B) Side and top views of the two interacting naphthyl groups (in space-filling mode). Symmetry operation: f = 1−x, −y, 2−z.

Compound **H2** crystallizes in the centrosymmetric space group *C*2/*c* (**Table S1**). Alike **H1**, **H2** is formed by two iron(III) ions coordinated by three doubly deprotonated $\mathbf{H_2L2}^{2-}$ ligands (**Figure 3**). The resulting neutral, triple-stranded helicate **H2** exhibits two octahedral metal centres with O6 donor sets produced by three β-diketonate units. The Fe−O bond lengths and O−Fe−O angles are comparable to those observed for **H1** (see **Table S2**).

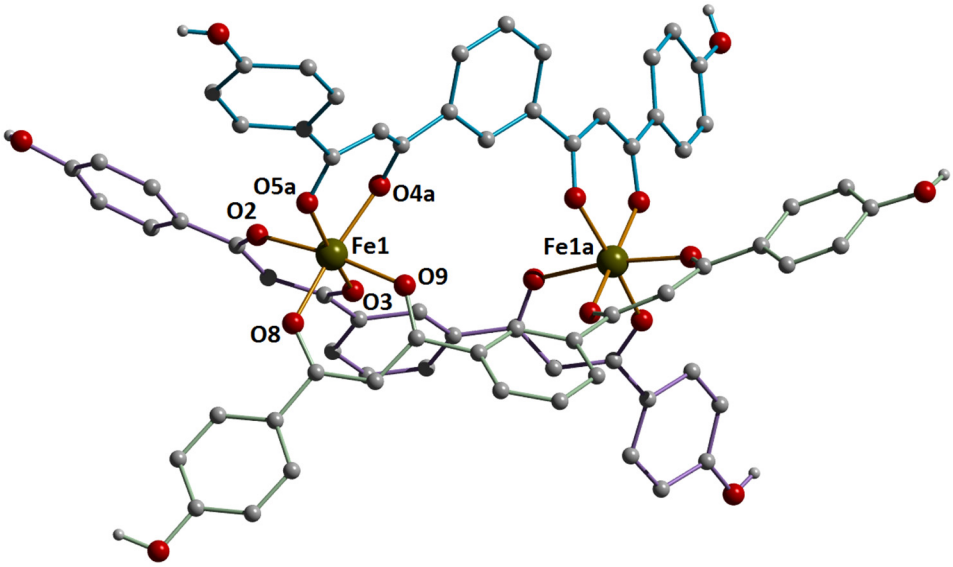

Figure 3. Representation of the crystal structure of **H2**. For clarity, solely the phenol hydrogen atoms are shown and the lattice solvent molecules are omitted. The three $\mathbf{H_2L2}^{2-}$ ligands are shown with different colours. Symmetry operation: a = 1−x, y, 1/2−z.

The crystal packing of **H2** shows that all phenolic O−H groups are involved in hydrogen-bonding interactions (**Figure 4** and **Table S3**), therefore fulfilling their expected role. The phenolic O6A−H6A group is interacting with a lattice water molecule (contact distance of 2.611(15) Å; **Figure 4A**), and the O7−H7 one with an acetonitrile solvent molecule (contact distance of 2.756(6) Å; **Figure 4B**). The phenolic O1−H1 group is involved in the formation of a supramolecular dimer of **H2**, through hydrogen bonds (O1−H1···O4 = 2.748(4) Å) and strong π−π interactions, as reflected by the observed short C1···C7 contact distance of 3.326(8) Å (**Figure 4C**).

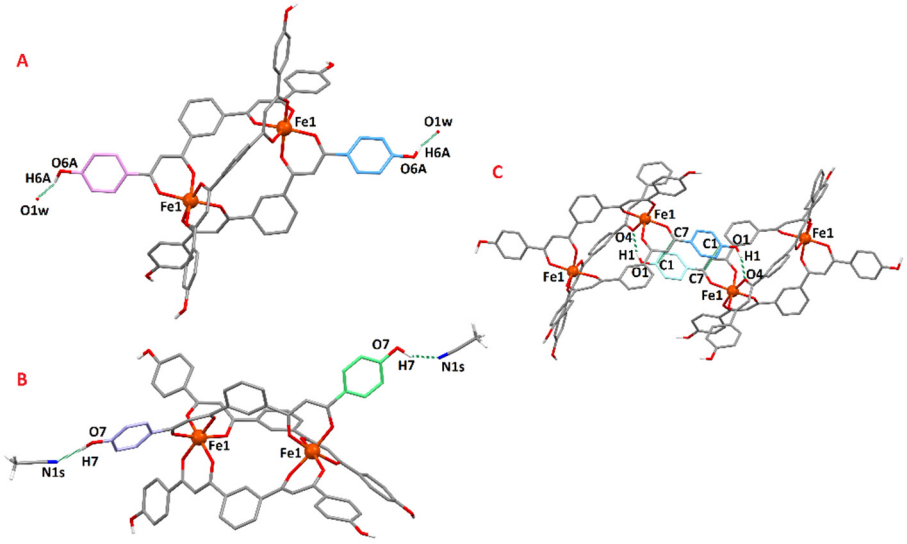

Figure 4. Representations of **H2** showing the involvement of the different phenol groups (identified by the respective oxygen atoms O6A, O7 and O1) in H-bonding interactions. A) Interaction with a lattice water molecule (O6A−H6A···O1w = 2.611(15) Å); B) Interaction with a lattice acetonitrile molecule (O7−H7···N1s = 2.756(6) Å); C) Interaction between neighbouring helicates (O1−H1···O4 = 2.748(4) Å and C1···C7 = 3.326(8) Å). For each case, the phenols involved are shown in various colours.

As observed for **H1** (see above), the solid-state structure of **H2** shows the presence of two conformers, in a 60:40 ratio (**Figure S3**). Again, it appears that the two different orientations exhibited by two phenolic groups (those involving the oxygen atom O6) are due to the occurrence of slightly distinct H-bonding contacts.

Interaction of H1, H2 and R2 with DNA

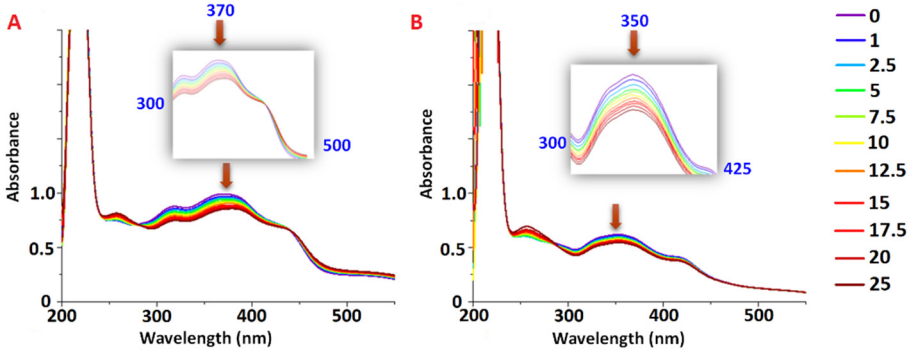

Figure 5. Absorption spectra of **H1** (A) and **H2** (B) in 1 mM sodium cacodylate/20 mM NaCl buffer upon addition of ct-DNA (0−25 μM). The insets show the respective zoom of the respective absorption region (MLCT band) used to determine the intrinsic binding constants K_b. The $[\text{ct-DNA}]_{bp}$ was determined from its absorption intensity at 260 nm, with a molar extinction coefficient of 6600 $M^{-1}cm^{-1}$ [37].

The DNA-binding properties of **H1** and **H2** (which are stable in solution; see the corresponding MALDI-TOF spectra in the Supporting Information file) were first investigated using UV-Vis spectroscopy. Titration experiments were thus carried out by recording absorption spectra at a constant complex concentration, namely 15 μM, without and with increasing amounts of *calf thymus* DNA (ct-DNA), *i.e.*[ct-DNA] = 0−25 μM (in base pair). The corresponding spectra for **H1** and **H2** are shown

in **Figure 5A** and **5B**, respectively. The binding abilities of **H1** and **H2** were assessed applying equation (1) [38,39]:

$$\frac{[DNA]}{(\varepsilon_a-\varepsilon_f)} = \frac{[DNA]}{(\varepsilon_b-\varepsilon_f)} + \frac{1}{K_b(\varepsilon_b-\varepsilon_f)} \quad (1)$$

where [DNA] is the concentration of DNA in base pair, ε_a is the apparent extinction coefficient obtained from A_{obs}/[complex], ε_f corresponds to the extinction coefficient of the DNA-free complex solution, and ε_b is the extinction coefficient of the DNA-bound complex solution. The ratio of the slope to the intercept from the plot of [DNA]/($\varepsilon_a - \varepsilon_f$) *vs.* [DNA] gives the K_b value. For **H1**, K_b amounts to 1.13 ± 0.13 x 10^5 M^{-1} (log K_b = 5.05), and it is 0.12 ± 0.07 x 10^5 M^{-1} (log K_b = 4.09) for **H2**. Thus, the naphthyl-containing iron cylinder **H1** is a more efficient DNA binder than **H2**. For both compounds, no significant red shift is observed upon addition of ct-DNA, which suggests that they are most likely acting through electrostatic interactions (outside binding) or/and as groove binders [40]. A slight red shift is noticed for **H1**, which may arise from a deeper groove binding of this compound (most likely involving its naphthyl groups), somewhat affecting base-pair stacks.

Fluorescence-dye displacement experiments were subsequently carried out using the intercalating agent ethidium bromide (EB). Bound to DNA, EB strongly fluoresces at λ_{em} = 610 nm (when excited at λ_{exc} = 514 nm). The fluorescence intensity of free EB decreases 20-fold [41]; the interaction of a molecule with DNA-EB may alter significantly the conformation of the double helix inducing the release of EB, which can be followed spectroscopically. Fluorescence spectra were recorded at constant concentrations of ct-DNA and EB (*i.e.* 25 and 125 µM, respectively), in the presence of increasing amounts of the supramolecular complex investigated. Emission spectra for EB in the presence of increasing quantities of **H1** and **H2** are shown in **Figure 6A** and **6B**, respectively.

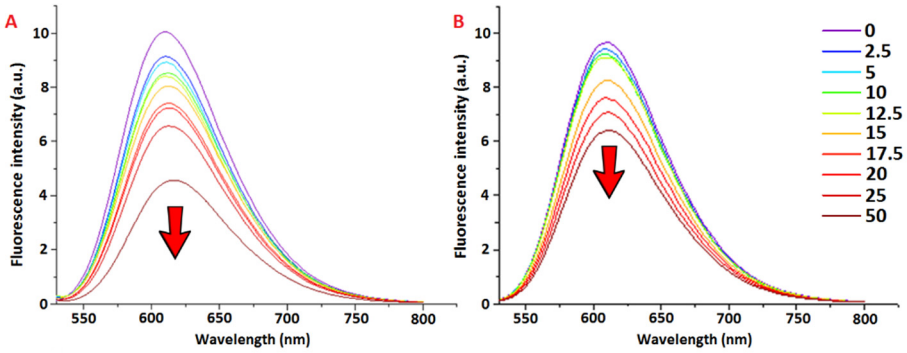

Figure 6. Emission spectra of DNA–EB (obtained using [ct-DNA] = 2.5 µM and [EB] = 12.5 µM) in 1 mM sodium cacodylate, 20 mM NaCl, λ_{exc}= 514 nm, λ_{em}= 610 nm, upon addition of increasing amounts of A) **H1** (2.5–50 µM) and B) **H2** (2.5–50 µM). The red arrows show the diminution of the emission intensity with the increase of complex concentration.

A clear and significant decrease in EB emission intensity is noticed, thus confirming the occurrence of strong interactions between the metallohelicates and ct-DNA. To evaluate the respective affinity of **H1** and **H2** for ct-DNA (compared to EB), their "quenching" efficiency was evaluated using the classical Stern-Volmer equation (2); by plotting I_0/I *vs.* [complex], the quenching constant K_{SV} can be determined [42].

$$\frac{I_0}{I} = 1 + K_{SV}[Q] \quad (2)$$

In equation (2), I_0 is the fluorescence intensity of the DNA bound to ethidium bromide and I is the fluorescence intensity upon the addition of each concentration of compound (*i.e.* the quenching molecule Q, which is **H1** or **H2** in the present study). The K_{SV} value of **H1** is 2.50 ± 0.07 × 10^5 M^{-1}, and that of **H2** amounts to 2.21 ± 0.12 × 10^5 M^{-1}. These data indicate that both compounds effectively displace EB;

electrostatic interactions or/and groove binding of these large supramolecules clearly are sufficient to induce a strong alteration of the structure of the biomolecule that gives rise to the release of the dye.
Competitive binding studies were also performed with the minor-groove binder Hoechst 33258 (**Figure S4**). Bound to ct-DNA, Hoechst 33258 fluoresces at λ_{em}= 458 nm when excited at λ_{exc}= 349 nm (for free Hoechst 33258, λ_{exc}= 337 and λ_{em} = 508 nm). The K_{SV} constants obtained for **H1** and **H2**, from the emission intensity decrease (**Figure S5**), are 19.33 ± 1.25 × 10^4 M^{-1} and 5.66 ± 0.28 × 10^4 M^{-1}, respectively. The stronger DNA interaction of **H1**, compared with that of **H2**, may be explained by stacking contacts of the naphthyl groups (of ligand **L1**) in the minor groove; partial intercalation of **H1** was also suggested by the UV-Vis data (slight red shift of the absorption; see above).
Charged molecules cannot diffuse through cell membranes; the passage of such molecules relies on specific transporters that are embedded in the membrane [43]. On the other hand, neutral (hydrophobic) molecules can pass through the lipid bilayer (if their size is not too large) [43]. To date, all DNA-binding metallohelicates that have been described in the literature are positively charged [44], most likely because the first one, reported by Hannon and co-workers, was cationic [16]. In the present study, neutral metallosupramolecular complexes have been developed, which are able to interact with the polyanionic double helix of DNA (see above). For comparison reasons, the DNA-binding properties of a tricationic helical complex, namely $Cl@[Fe_2(C_{22}H_{16}N_6)_3]Cl(PF_6)_2$ (**R2**) (**Figure S1**), have been investigated as well. **R2** has been used for a completely different purpose, *viz.* for its spin-crossover properties [34]; hence, its biological properties have not been studied so far (*viz.*, its DNA-interacting properties have not been reported until now). It can also be pointed out here that the ligand of **R2** is obtained from a bis-β-diketone, by reaction with hydrazine (**Figure S6**).
The DNA-binding abilities of **R2** were assessed by UV-Vis and fluorescence spectroscopy. The absorption data illustrated in **Figure S7A** were used to determine the intrinsic binding constants K_b, applying equation (1). The K_b value of 15.3 ± 0.07 × 10^5 M^{-1} (log K_b = 6.18) indicates that the DNA-binding affinity of **R2** is clearly higher than those of **H1** and **H2**. EB-displacement studies corroborate this trend (**Figure S7B**); the quenching constant K_{SV} of 3.14 ± 0.21 × 10^5 M^{-1}, obtained from equation (2), again shows a stronger interaction of **R2** with DNA, compared with that of **H1** or **H2**.
It can be mentioned here that the tetracationic helicate of reference, namely **R1**, designed by Hannon and co-workers [16], shows a DNA-binding constant K_b, determined by EB-displacement assay [17], in the range of 10^7 M^{-1}. Hence, this constant is one order of magnitude higher than that of tricationic **R2** (K_b = 1.53 × 10^6 M^{-1}), and two-three orders of magnitude higher than those of neutral **H1** and **H2** (1.13 × 10^5 M^{-1} and 1.20 × 10^4 M^{-1}, respectively). It thus appears that the compound exhibiting the greatest positive charge, namely **R1**, exhibits the strongest affinity with the negatively-charged biomolecule.

Cell-viability assays

The cellular toxicity of **H1**, **H2** and **R2** was first evaluated using single-point assays. Various cell lines (representing common cancers) were screened, namely A549 (lung adenocarcinoma), A375 (melanoma), MCF-7 (breast adenocarcinoma), SKOV3 (ovary adenocarcinoma), SW620 (colorectal adenocarcinoma) and PC3 (prostate adenocarcinoma). The cell viabilities were determined for each compound after an incubation time of 24 hours at 37 °C. Two different concentrations of supramolecular complex were used, *viz.* 10 and 50 μM. The corresponding percentages of living cells are shown in **Figure 7** and are listed in **Table 1**.
Compound **H2** is not cytotoxic; cell viabilities ≥ 92% are observed in all cell lines (**Table 1**, entries 1-6), even at a complex concentration of 50 μM (**Table 1**; entries 7-12); this lack of activity may arise from the impossibility for **H2** to enter the cells. In contrast, metallohelicate **H1** shows some interesting activities, particularly against colorectal cells; at [**H1**] = 10 μM, only 5% of the cells are still alive after an incubation time of 24 hours (**Table 1**, entry 4). It appears that **H1** is highly selective towards SW620 cells (**Table 1**, entries 4 and 10); at [**H1**] = 50 μM, only the melanoma cells A375 (in addition to SW620 cells; **Figure 7B** and **Table 1**, entry 8) seem to be affected. Compared to **H1** and **H2**, the activity of **R2** is slightly better; indeed, at [**R2**] = 10 μM, two cell lines are affected, namely the SW620 colorectal and PC3 prostate lines (**Table 1**; entries 4 and 6), and almost all cells are affected when a concentration [**R2**] = 50 μM is used (**R2** is not cytotoxic to lung cells A549; **Table 1**, entry 7). It can be noticed that the cytotoxicity follows the tendency observed with the DNA-binding studies (see above), *viz.* **R2** > **H1** > **H2**.

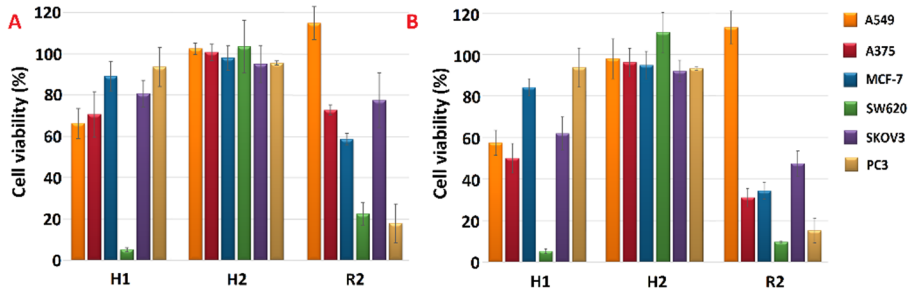

Figure 7. Cell viability data (%) after 24 h incubation at 37 ºC, obtained for **H1**, **H2** and **R2** with six cancer cell lines, namely A549 (lung adenocarcinoma), A375 (melanoma), MCF-7 (breast adenocarcinoma), SKOV3 (ovary adenocarcinoma), SW620 (colorectal adenocarcinoma) and PC3 (prostate adenocarcinoma); A) [compound] = 10 μM and B) [compound] = 50 μM. The viabilities (in %) shown are mean values ± SD of three independent experiments.

Table 1. Cell-viability assays (single-point screening, % cell viability) for **H1**, **H2** and **R2** with different cancer cell lines, namely A549 (lung adenocarcinoma), A375 (melanoma), MCF-7 (breast adenocarcinoma), SKOV3 (ovary adenocarcinoma), SW620 (colorectal adenocarcinoma) and PC3 (prostate adenocarcinoma). Two complex concentrations were used, *i.e.* 10 and 50 μM, and an incubation time of 24 hours at 37 ºC was applied. The viabilities (in %) shown are mean values ± SD of three independent experiments. % cell viability ≤ 50 % are highlighted in grey; the best values for **H1** and **R2** are highlighted in dark grey.

		[Compound] = 10 μM		
Entry	Cell line	**H1**	**H2**	**R2**
1	A549	66.3 ± 7.30	103 ± 2.76	115 ± 7.92
2	A375	70.7 ± 11.0	101 ± 3.96	72.9 ± 2.46
3	MCF-7	89.2 ± 7.19	98.1 ± 5.91	58.8 ± 2.86
4	SW620	5.07 ± 0.97	104 ± 12.7	22.5 ± 5.34
5	SKOV3	80.7 ± 6.53	95.1 ± 9.00	77.6 ± 13.3
6	PC3	93.7 ± 9.45	95.6 ± 0.99	17.8 ± 9.45
		[Compound] = 50 μM		
	Cell line	**H1**	**H2**	**R2**
7	A549	57.5 ± 5.96	97.9 ± 9.60	113 ± 7.92
8	A375	50.1 ± 7.15	96.2 ± 6.82	31.1 ± 4.31
9	MCF-7	84.2 ± 4.14	94.9 ± 6.61	34.3 ± 4.06
10	SW620	5.28 ± 1.05	111 ± 9.70	9.6 ± 0.57
11	SKOV3	61.9 ± 7.99	92.0 ± 5.20	47.4 ± 6.19
12	PC3	93.7 ± 9.45	93.3 ± 0.78	15.1 ± 5.86

Considering the results obtained, inhibitory-concentration values were determined for compounds **H1** and **R2** with SW620 cells. For comparison, inhibitory concentrations were also determined for two reference compounds, namely Mike Hannon´s helicate **R1** [16] and cisplatin, under the same experimental conditions (*i.e.* the four compounds were tested simultaneously). The corresponding $IC_{25\text{-}75}$ values (in μM), obtained after 24 h incubation at 37 ºC, are listed in **Table 2**.

Table 2. $IC_{25\text{-}75}$ values (μM) obtained for **H1**, **R2**, **R1** and cisplatin with SW620 cells, after incubation of 24 hours at 37 ºC. The data shown are means ± SD of three independent experiments. The IC_{50} values are shown in bold.

	H1	**R2**	**R1**	cisplatin
IC_{25}	4.4 ± 0.7	2.9 ± 0.8	38.0 ± 4.6	18.0 ± 2.5
IC_{50}	**9.4 ± 1.4**	**11.0 ± 1.5**	**64.0 ± 5.7**	**45.0 ± 6.4**
IC_{75}	23.0 ± 1.6	41.0 ± 5.3	89.0 ± 6.7	96 ± 14

Remarkably, the two newly-studied metallocylinders **H1** and **R2** are significantly more active than the reference metallohelicate **R1** [16]; they are also more cytotoxic than the clinical drug cisplatin for this cell line (under the same experimental conditions). Interestingly, the neutral supramolecular compound **H1** is the most efficient agent against this cell line; it is seven times more active than the well-known, cationic helicate **R1** (**Table 2**). These data therefore illustrate the potential of using neutral helicates as antiproliferative agents.

Cell studies

Confocal-microscopy studies were subsequently carried out to find out whether **H1** and **R2** could reach the cell nucleus, and possibly induce cell apoptosis. Hence, the nucleus of SW620 cells was stained with a fluorescent dye, *viz*. TO-PRO™-3 iodide. It generates a very bright blue fluorescence signal upon binding to DNA, giving a strong and selective nuclear staining in cultured cells. Any nuclear anomalies can be detected, such as the formation/presence of apoptotic bodies or the deformation of nuclei. Fluorescence microscopy images of nucleus-stained SW620 cells were taken after 48 hours incubation with **R1**, **H1** and **R2** (see **Figures 8** and **S8**).

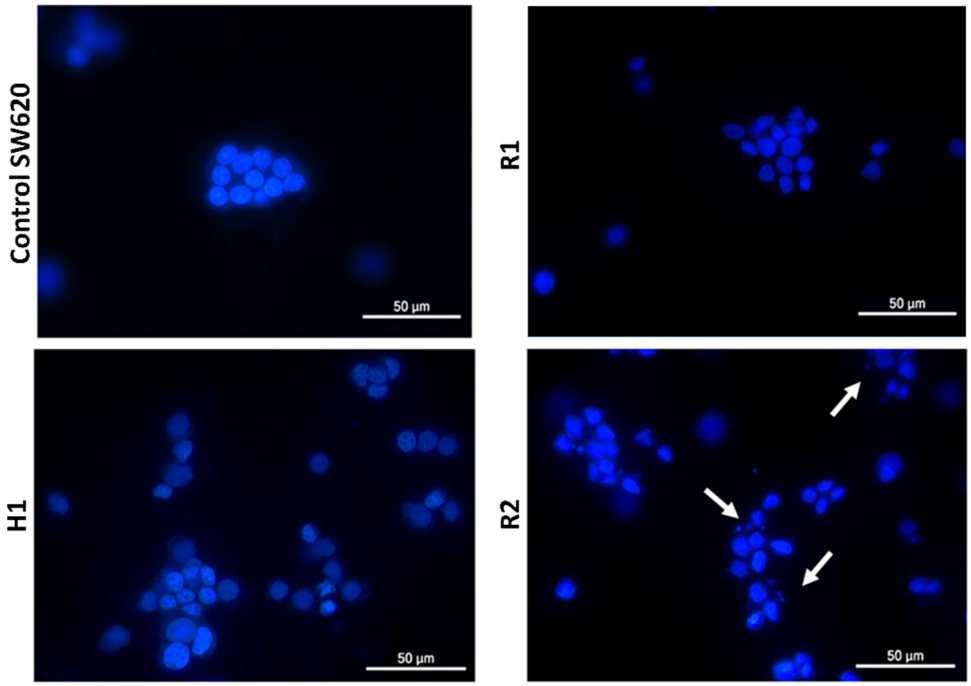

Figure 8. Confocal microscopy images showing the blue-stained nucleus of SW620 cells, SW620 cells incubated with **R1**, **H1** and **R2** [this compound is affecting the nucleus of SW620 cells; apoptotic bodies are clearly seen (white arrows)]. The concentrations of each compound used correspond to the corresponding IC_{25} values (see **Table 2**). The selected images are representative of three distinct series of images. Incubation time = 48 h; scale bar = 50 µm.

Although **H1** exhibits the best IC_{50} value, it does not seem to (significantly) affect/reach the nucleus of SW620 cells (see control cells and SW620 cells incubated with **H1** in **Figure 8**). In fact, the same behavior is observed with the reference metallohelicate **R1**. Thus, it appears that the mechanism of action of **H1** does not involve its binding to DNA. Additional experiments are however required to further confirm this assumption, and to determine what is the cellular target of **H1** (in SW620 cells) that leads to cell death. In contrast, the microscopy image obtained with **R2** suggests that this compound is affecting the nucleus of SW620 cells; apoptotic bodies are seen (white arrows), therefore indicating that the cell-death mechanism of **H1** and **R2** are distinct.

Cell-cycle analyses by quantitation of DNA content using flow cytometry were then performed with SW620 cells incubated for 24 hours with **H1** and **R2**. The results achieved, giving quantitative information regarding the amounts (percentages) of cells in the G_0/G_1, S and G_2/M phases, are depicted in **Figure 9**.

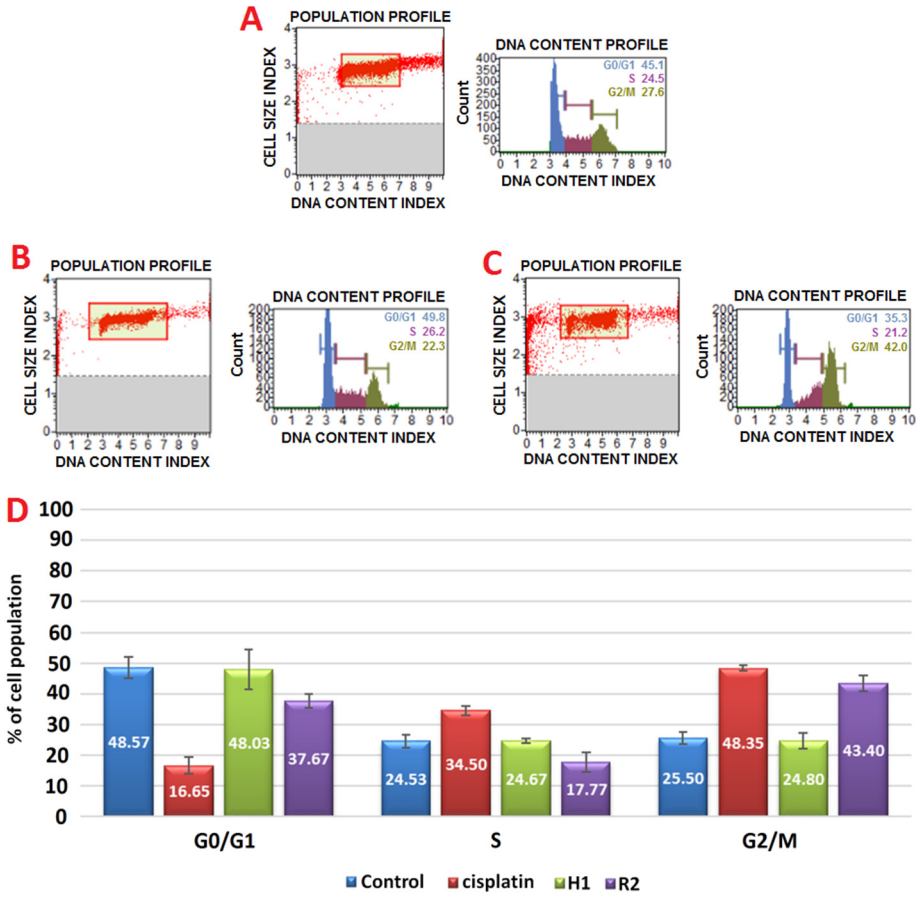

Figure 9. Cell-cycle analyses of SW620 cells A) without compound added; B) incubated for 24 hours with **H1**; C) incubated for 24 hours with **R2**. D) Histograms showing the percentages of cells in the G_0/G_1, S and G_2/M phases of the cell cycle. 2×10^5 cells mL^{-1} was used for sorting; [compound] =2 μM. The results are representative of three independent experiments.

As already observed by confocal microscopy, **H1** is not affecting the "DNA cycle"; the percentages of SW620 cells in each phase is comparable with those of untreated cells (see blue and green bars in **Figure 9**). On the contrary, **R2** clearly arrests the cell cycle (see red bars in **Figure 9**); for instance, 48% of the SW620 cells are arrested at the G_2/M phase, an amount that is like that achieved with cisplatin (see red and purple bars in the G_2/M phase; **Figure 9**). It is known that upon G_2/M arrest, some essential mitotic processes are altered; the resulting incomplete mitosis/mitotic catastrophe leads to cell death [45]. **R2** appears to trigger cell apoptosis, which is not the case for **H1**.

III. Conclusions

In the present study, iron(III) metallohelicates **H1** and **H2** have been prepared from bis-β-diketone ligands containing distinct functional groups, *viz*. naphthyl moieties aimed at favoring π-stacking interactions with DNA base pairs and phenol groups for their potential interactions with the double helix backbone or/and nitrogenous bases. The DNA-interacting properties of the neutral metallohelicates obtained were evaluated, which revealed that both metallocylinders could interact and disturb the structure of the

biomolecule, mostly through groove binding; the naphthyl-containing supramolecule **H1** is better interacting with DNA (most likely due to its partial intercalation) than phenol-containing **H2**. For comparison, the DNA-binding properties of a tricationic iron(II) helicate reported in the literature (for its spin crossover properties), namely compound **R2**, were examined. This positively charged metallocylinder shows higher affinity for the polyanionic biomolecule than **H1** and **H2**. However, cell viability studies with six different cancer cell lines revealed that neutral **H1** is very active against colorectal SW620 cells, more than **R2**; **H2** is not active at all in all cell lines tested. Moreover, both **H1** and **R2** are significantly more cytotoxic towards SW620 cells than two very well-known compounds, namely tetracationic metallohelicate **R1** that is the reference compound in the field, and cisplatin, which is one of the most used anticancer drugs. Confocal microscopy and cell cycle studies showed that, while **H1** does not seem to affect the nucleus of SW620 cells, **R2** apparently can reach the nucleus (most likely producing apoptotic bodies) and arrest the cell cycle at the G_2/M phase, hence suggesting that it can trigger apoptosis.
In summary, the data achieved allowed to reveal the potential of two families of coordination helicates, represented by compounds **H1** and **R2**, for the design and development of efficient antiproliferative agents. In particular, the study has shown that neutral metallocylinders may display interesting DNA-binding and cytotoxic properties. The different biological (cellular) behavior exhibited by **H1**, **H2** and **R2** may be explained by (i) the ability of **H1** to target a cellular component (that should be identified), (ii) the likely inability of **H2** to enter the cell, and (iii) the apparent pro-apoptotic properties of **R2**. More in-depth studies are obviously required to clarify the distinct mode of action of metallosupramolecular compounds.

IV. Additional Information

Supporting information is available online. Representations of the crystal structures of **R1** and **R2**; crystal data and structure refinement for **H1** and **H2**; selected bond lengths and angles **H1** and **H2**; selected contact distances for **H1** and **H2**; representations of the lattice conformers of **H1** and **H2**; schematic representation of Hoechst 33258; fluorescence spectra related to competitive binding studies between **H1** and **H2** and Hoechst 33258; UV-Vis and fluorescence spectra for the competitive binding studies with **R2**; confocal microscopy images of SW620 cells treated with **H1**, **R1** and **R2**; ^{1}H NMR spectra for ligands $\mathbf{H_2L1}$ and $\mathbf{H_4L2}$. Correspondence and requests for materials should be addressed to P.G.

V. Materials and Methods

General. Dimethyl isophthalate, sodium hydride (60% dispersion in mineral oil), 1,2-dimethoxyethane (≥ 99%), 2-acetonaphthone, 4'-hydroxyacetophenone (99%), iron(III) chloride hexahydrate, sodium cacodylate, *cis*-diamminedichloridoplatinum(II) (cisplatin), DMSO (for molecular biology), penicillin-streptomycin (BioReagent), L-glutamine (BioXtra), DMEM-F12 (Ham), 3-(4,5-dimethylthiazol-2-yl)-2,5-diphenyltetrazolium bromide (MTT), sodium pyruvate, insulin, paraformaldehyde and phosphate buffered saline (PBS) were purchased from Sigma-Aldrich and were used as received. Ethanol, HCl 37%, dichloromethane, sodium hydrogen carbonate, sodium sulfate anhydrous, sodium chloride and tetrahydrofuran were purchased from Fisher Scientific and were used as received. *Calf thymus* DNA was obtained from Sigma-Aldrich. All specific reagents used for the *in vitro* DNA-interaction studies, *e.g.* ethidium bromide and Hoechst 33258, were obtained from Sigma-Aldrich and Invitrogen. Nuclear magnetic resonance (NMR) spectra were recorded at 298 K on a Varian Mercury 400 MHz spectrometer. Chemical shifts (δ) are reported in parts per million (ppm) and are referenced to the nondeuterated solvent peak ($CHCl_3$: 7.26 ppm). IR spectra were recorded in KBr using a Nicolet-5700 FT-IR (in the range 4000–400 cm^{-1}), and the main absorption bands are reported (cm^{-1}). Electrospray ionization (ESI) mass spectrometry was carried out with an LC/MSD-TOF spectrometer from Agilent Technologies equipped with an ESI source, at the Centres Científics i Tecnològics de la Universitat de Barcelona. The samples were eluted with a H_2O/CH_3CN 1:1 mixture and measured in the positive mode. MALDI (matrix-assisted laser desorption ionization) experiments were performed using a 4800 Plus MALDI-TOF/TOF spectrometer at the Unitat d'Espectrometria de Masses of the Universitat de Barcelona. The samples (helicates **H1** and **H2**) were dissolved in the minimum of DMSO and diluted with methanol before the measurement. C, H, and N elemental analyses were performed at the Centres Científics i Tecnològics de la Universitat de Barcelona, using a Thermo EA 1108 CHNS/O analyzer from Carlo Erba Instruments. Spectroscopic measurements (DNA-binding studies) in buffered aqueous media were done in cacodylate buffer solution (1 mM sodium cacodylate, 20 mM NaCl, pH 7.2), prepared with ultrapure water and whose

pH was adjusted with aqueous HCl. The concentration of ct-DNA was determined from its absorption intensity at 260 nm with a molar extinction coefficient of 6600 $M^{-1}cm^{-1}$. The DNA purity was assessed by determining the 260 nm/280 nm ratio (a ratio around 1.8–1.9 indicates that the DNA used is sufficiently protein free). UV-Vis and fluorescence spectra were collected in 1 cm path length quartz cuvettes, using a Varian Cary-100 spectrophotometer and a KONTRON SFM 25 spectrofluorometer, respectively.

Preparation of ligand H_2L1. Dimethyl isophthalate (2.9 g, 15 mmol) was added to a suspension of 60% sodium hydride (oil dispersion, 3 g, 75 mmol) in 150 mL of 1,2-dimethoxyethane (DME); the resulting mixture was stirred for 15 minutes. Subsequently, a solution of 2-acetonaphthone (5.1 g, 30 mmol) in 50 mL of DME was added dropwise, and the reaction mixture was heated under reflux for 4 h. The yellow-mustard suspension obtained was quenched by addition of 5 mL of ethanol (to neutralize the excess of sodium hydride). The solid was collected by filtration and then re-suspended in 150 mL of water. The pH was adjusted to 2–3 using 12 % HCl, and the acidified aqueous phase was stirred for 30 minutes. The yellow solid obtained, *i.e.* **H_2L1**, was collected by filtration, washed with water, and dried under vacuum. Yield: 5.47 g (77%). ^{1}H NMR (400 MHz, $CDCl_3$): δ = 8.67 (s, 1H), 8.59 (s, 2H), 8.23 (d, 2H), 8.08−7.90 (d+d+d+d 8H), 7.68 (t, 1H), 7.70−7.56 (t+t, 4H), 7.10 (s, 2H($C-H_{enol}$)) ppm (**Figure S9**). IR (KBr, cm^{-1}): 3550, 3474, 3415, 3054, 1606, 1532, 1385, 1302, 1189, 1061, 781, 769 (**Figure S11**). Anal. Calcd. for $C_{32}H_{22}O_4$: C, 81.69; H, 4.71. Found: C, 81.28; H, 4.63. MS (ESI$^+$): m/z = 471.15 $[M+H]^+$.

Preparation of ligand H_4L2. Dimethyl isophthalate (5 g, 26 mmol) was added to a suspension of 60% sodium hydride (oil dispersion, 8.8 g, 220 mmol) in 150 mL of DME. The resulting mixture was stirred for 15 minutes and a solution of 4'-hydroxyacetophenone (7.1 g, 52 mmol) in 50 mL of DME was added dropwise. The reaction mixture was heated under reflux overnight and the excess of NaH was quenched by addition of 5 mL of ethanol. The yellow solid was isolated by filtration and re-suspended in 200 mL of HCl 0.1 M. 200 mL of dichloromethane (DCM) were added and the biphasic system was vigorously stirred for 1 hour. The organic phase was collected, and the aqueous phase was extracted twice with 200 mL of DCM. The combined organic phase was dried over Na_2SO_4, filtered and evaporated under reduced pressure. The solid material was re-dissolved in the minimum of refluxing ethanol. Upon cooling, **H_4L2** was obtained as a yellow material, which was isolated by filtration and dried under reduced pressure. Yield: 6.7 g (64%). ^{1}H NMR (400 MHz, d_6-DMSO): δ = 9.88 (br s, 2H, OH_{phenol}, 8.73 (s, 1H), 8.41 (d, 2H), 7.76 (t, 1H), 7.68 (d, 2H), 7.54 (s, 2H($C-H_{enol}$)), 7.37 (m, 4H), 7.07 (d, 2H) ppm (**Figure S10**). IR (KBr, cm^{-1}): 3390, 3080, 2920, 2850, 1688, 1608, 1574, 1488, 1452, 1308, 1281, 1237, 1061, 762, 727 (**Figure S11**). Anal. Calcd. for $C_{24}H_{18}O_6$: C, 71.64; H, 4.51. Found: C, 71.42; H, 4.63. MS (ESI$^+$): m/z = 403.11 $[M+H]^+$.

Preparation of supramolecular complexes H1 and H2. Six equivalents of sodium hydrogen carbonate were slowly added to a solution of three equivalents of ligand in 30 mL of tetrahydrofuran (THF). Next, a solution of two equivalents of $FeCl_3 \cdot 6H_2O$ in THF (20 mL) was slowly added. The resulting reaction mixture was refluxed for 45 minutes, and subsequently filtered (to remove any insoluble impurities). The dark-red solutions of complexes were used for crystallization experiments. Dark-red, needle-like single crystals, suitable for X-ray diffraction analysis, were obtained applying the "solvent layering" technique.

$[Fe(L1)_3](MeCN)(THF)_{0.25}$ (H1). Obtained in THF/acetonitrile solvent layers (complex in acetonitrile) using 50 mg (0.106 mmol) of ligand **H_2L1**. Yield: 104 mg (62% based on **H_2L1**). MALDI-TOF MS: m/z 1517.4 $[Fe(\mathbf{L1})_3]^+$ (**Figure S12**). IR (KBr, cm^{-1}): 3425, 3054, 1628, 1597, 1525, 1484, 1417, 1369, 1342, 1316, 1102, 1060, 789 (**Figure S14**). Anal. Calcd. for $C_{99}H_{65}Fe_2NO_{12}$ (compound without THF): C, 75.63; H, 4.17; N, 0.89 Found: C, 76.22; H, 4.60; N, 1.19.

$[Fe(H_2L2)_3](MeCN)_2(H_2O)_2$ (H2). Obtained in THF/acetonitrile solvent layers (complex in acetonitrile) using 100 mg (0.248 mmol) of ligand **H_4L2**. Yield: 135 mg (38% based on **H_4L2**). MALDI-TOF MS: m/z 1313.2 $[Fe(\mathbf{L2})_3]^+$ (**Figure S13**). IR (KBr, cm^{-1}): 3347, 1692, 1605, 1529, 1482, 1420, 1362, 1306, 1242, 1065, 783 (**Figure S14**). Anal. Calcd. for $C_{76}H_{58}Fe_2N_2O_{20}$: C, 63.79; H, 4.09; N, 1.96 Found: C, 64.31; H, 4.45; N, 1.39.

The synthesis and crystal structure of metallohelicates $[Fe_2(C_{25}H_{20}N_4)_3]Cl_4$ (**R1**) [17] and $Cl@[Fe_2(C_{22}H_{16}N_6)_3]Cl(PF_6)_2$ (**R2**) were reported by Vellas *et al.* [46] and Darawsheh *et al.* [34], respectively.

X-ray structure determination. Data for compounds **H1** and **H2** were collected on a Bruker APEXII diffractometer at beamline 11.3.1 of the Advanced Light Source synchrotron (λ = 0.7749 Å), at 100 K respectively on 0.20 × 0.04 × 0.03 mm^3 and 0.06 × 0.02 × 0.01 mm^3 red needles. In the case of **H1**, no single crystals could be found, and the data were collected on a non-merohedral twin. The orientation matrices were determined by CELL_NOW [47] that ascribed reflections to either or both components. Cell refinement and integration were done with SAINT [47], as a 2-component twin for **H1**, keeping the cell of both components identical. Absorption corrections for **H2** were done with SADABS [48], while those for **H1** were done with TWINABS [47] that produced an HKLF4 file for structure solution and initial refinement, and an HKLF5 file for the final refinement. The structures of **H1** and **H2** were solved respectively by direct methods with SHELXS [49] and intrinsic phasing with SHELXT [49] and refined by full-matrix least-squares on F^2 with SHELXL [49]. In **H1**, one of the naphthyl groups is disordered over two positions rotated by 180º, while a second naphthyl group has its outer aromatic cycle also disordered over two positions. In **H2**, one of the phenol groups is also disordered over two positions. All details can be found in CCDC 1840212 (**H1**) and 1840213 (**H2**) that contain the supplementary crystallographic data for this paper. These data can be obtained free of charge from the Cambridge Crystallographic Data Center via https://summary.ccdc.cam.ac.uk/structure-summary-form. Crystallographic and refinement parameters are summarized in **Table S1**. Selected bond distances and angles and contact distances are given in **Tables S2** and **S3**, respectively.

Ethidium bromide displacement assays. Samples containing ct-DNA (2.5 µM, in base pair) and ethidium bromide (EB; 12.5 µM) in cacodylate buffer (1 mM sodium cacodylate, 20 mM NaCl, pH = 7.2) were incubated at 37 °C for 1 h. The ratio of ct-DNA/EB of 1:5 was determined by fluorescence spectroscopy and corresponds to the saturation of the EB emission signal (λ_{exc} = 514 nm; λ_{em} = 610 nm). Subsequently, the samples were treated with increasing concentrations of the complex, *i.e.* 0−50 µM (see **Figure 6**), obtained from a stock solution of 5 mM (freshly prepared in DMSO before each experiment and diluted in cacodylate buffer). The resulting samples, containing up to 5% DMSO in a final volume of 3 mL, were then incubated at 37 °C for 24 h. Afterwards, the fluorescence emission spectra of all samples were recorded at room temperature in the range 530-800 nm (see **Figure 6**). Solutions of ct-DNA/EB without complex were used as controls.

Hoechst 33258 displacement assays. These displacement assays were carried out as above using [ct-DNA] = 0.19 µM (in base pair) and [Hoechst 33258] = 15 µM in cacodylate buffer (ratio of ct-DNA/ Hoechst 33258 of 1:79 determined by fluorescence spectroscopy). Complex concentrations in the range 2−150 µM were used and the fluorescence emission spectra (emission of Hoechst 33258; λ_{exc} = 349 nm; λ_{em} = 458 nm) were recorded at room temperature in the range 350-650 nm (see **Figure S5**). Solutions of ct-DNA/Hoechst 33258 without complex were used as controls.

Cell lines and culture. Human lung adenocarcinoma (A549), melanoma (A375), breast adenocarcinoma (MCF7), colorectal adenocarcinoma (SW620), ovarian adenocarcinoma (SKOV3), and prostate adenocarcinoma (PC3) cell lines used in this study were purchased from the American Type Culture Collection (ATCC). All cell lines were tested and authenticated by ATCC using short tandem repeat analysis and were cultured (passage number 10−25) following ATCC recommended media. A549, A375, SKOV3 and SW620 cells were cultured in Dulbecco's Modified Eagle's Medium (DMEM) medium (Sigma-Aldrich) supplemented with 10% (v/v) fetal bovine serum (FBS; Life Technologies, Carlsbad, CA, USA), 100 U mL^{-1} penicillin, 100 µg mL^{-1} streptomycin, and 2 mM L-glutamine. MCF7 and PC3 cells were cultured in DMEM-F12 (Ham) supplemented with 5% horse serum (v/v) (Life Technologies), 100 µM sodium pyruvate, 10 µg/mL insulin, 100 unit/mL penicillin, 100 µg/mL streptomycin, and 2 mM L-glutamine. All cell lines were grown at 37 ºC under a 5% CO_2 atmosphere. The cell lines were routinely tested using a specific standard PCR to control mycoplasma contamination.

Cell viability assays. Cell proliferation was evaluated by the 3-(4,5-dimethylthiazol-2-yl)-2,5-diphenyltetrazolium bromide (MTT) assay. Cells (1 × 10^5 cells per mL; 100 µL) were seeded in 96-well plates and allowed to grow for 24 h. After attachment to the surface, the cells were then incubated for 24 hours at 37 ºC, with various concentrations of **H1**, **H2** and **R2** (*i.e.* 10 and 50 µM for the single-point experiments and in the range 1−100 µM for the dose−response curves), which were freshly dissolved in DMSO and subsequently diluted in the corresponding culture medium (final [DMSO] ≤ 1%). Control cells

were cultured in the corresponding culture medium plus the carrier (DMSO; final concentration ≤ 1%). Following the treatment, 10 μM MTT was added to each well, and the cells were incubated for an additional 4 h. Afterward, the medium was aspirated, and the blue formazan precipitate was dissolved in 100 μL of DMSO. The absorbance was measured at 570 nm in a multi-well plate reader (Multiskan FC, Thermo Scientific). The cell viability was expressed as percentage values with respect to control cells, and the data are shown as the mean value ± standard deviation (SD) of three independent experiments. The dose−response curves and the corresponding half maximal inhibitory concentration (IC_{50}) were obtained by means of nonlinear regression (curve fit) calculated with the GraphPad Prism 5.0 software (GraphPad Software, San Diego, CA, USA). For comparison purposes, the cytotoxic effects of cisplatin and $[Fe_2(C_{25}H_{20}N_4)_3]Cl_4$ (**R1**) were also evaluated under the same experimental conditions.

Confocal microscopy. SW620 cells (2×10^5 cells mL^{-1}) were cultured in a 12-well plate containing glass coverslips and were incubated for 24 and 48 h, with IC_{25} concentrations of the compounds investigated (see **Table 2**). The cells were subsequently washed with 1 × PBS and fixed with 4% paraformaldehyde in PBS, during 20 minutes at room temperature. The fixed cells were permeabilized with 0.2% Triton™ X-100 (Sigma-Aldrich) and the coverslips were washed twice with 1 × PBS. The cells were then treated for 2 h at room temperature with blocking solution (PBS-Tween-20 0.1%, 0.1% Bovine Serum Albumin, and 10% normal goat serum). Subsequently, the cells were incubated for 1 h with the nuclear marker TO-PRO™-3 iodide (1:400, Cat T3605, Molecular Probes). Next, the coverslips were washed with PBS and placed on slides with Mowiol (Sigma-Aldrich, St. Louis, MO, USA). The fluorescence microscopy images were captured using a Leica TCS-SL filter-free spectral confocal microscope (Leica Microsystems). Several independent experiments were performed, and the fluorescence intensities (n = 30/condition) were normalized and quantified using the ImageJ software.

Cell cycle studies. SW620 cells (2×10^5 cells mL^{-1}) were cultured in a 6-well plate and subsequently incubated for 24 hours at 37 ºC with with IC_{50} concentrations (see **Table 2**) of the studied compounds. The cells were then trypsinized, collected and centrifuged at 300 × g for 5 minutes. The supernatant was discarded without disturbing the cell pellets. An appropriated volume of PBS was added to each tube to obtain a concentration of 1×10^6 cells mL^{-1}. After centrifugation at 300 × g for 5 minutes, the supernatant was removed and discarded without disturbing the cell pellets. Approximately 50 μL of PBS per 1×10^6 cells were added and the pellets were resuspended. The resuspended cells were added drop-wise into a tube containing 1 mL of ice-cold ethanol (70%), while vortexing at medium speed. The samples were then freezed at –20 °C for at least 3 hours prior to staining. 200 μL of ethanol-fixed cells were recovered and centrifuged at 300 × g for 5 minutes at room temperature. The supernatant was removed and discarded without disturbing the cell pellets. Approximately 250 μL of PBS were added to obtain a cell concentration of around 5×10^5 cells mL^{-1}. This step was repeated to eliminate all the fixing solution. The cell pellets were resuspended in 200 μL of Muse™ Cell Cycle Reagent and incubated for 30 minutes at room temperature, protected from light. The suspension was transferred into a 1.5-mL microcentrifuge tube prior to analysis with a Muse™ Cell Analyzer. The results are expressed as the mean ± SEM of at least three independent experiments. One-way ANOVAs were carried out with the Statgraphics centurion statistical package and post-hoc Tukey analyses were performed.

VI. Conflict of Interests

The authors declare there are no conflict of interests.

VII. Acknowledgements

Financial support from the Spanish Ministerio de Ciencia Innovación, y Universidades (Project nos. CTQ2015-70371 and CTQ2017-88446-R AEI/FEDER, UE) is acknowledged. This work was also partially supported by a grant from the Spanish government and the EU (FIS PI13/00089) and a grant from La Marató TV3 (20132730). L.K.G is thankful to a program from the University of Barcelona in collaboration with Obra Social de la Fundación Bancaria "La Caixa" for an individual contract. This research used resources of the Advanced Light Source, which is a Department of Energy Office of Science

User Facility under Contract No. DE-AC02-05CH11231. Guillem Aromí is thanked for providing a sample of $Cl@[Fe_2(C_{22}H_{16}N_6)_3]Cl(PF_6)_2$ (**R2**).

VIII. References

[1] Baselga J., Bhardwaj N., Cantley L. C., DeMatteo R., DuBois R. N., Foti M., Gapstur S. M., Hahn W. C., Helman L. J., Jensen R. A., Paskett E. D., Lawrence T. S., Lutzker S. G., Szabo E., *Clin. Cancer Res.* **2015**, *21*, S1-S128.

[2] Torre L. A., Siegel R. L., Ward E. M., Jemal A., *Cancer Epidemiol. Biomarkers Prev.* **2016**, *25*, 16-27.

[3] Sanchez-Cano C., Hannon M. J., *Dalton Trans.* **2009**, 10702-10711.

[4] Cooley M. E., Davis L. E., Destefano M., Abrahm J., *Cancer Nurs.* **1994**, *17*, 173-184.

[5] Lippert B. *Cisplatin, Chemistry and Biochemistry of a Leading Anti-Cancer Drug*. Wiley-VCH: Weinheim, **1999**.

[6] Barnard C. F. J., Cleare M. J., Hydes P. C., *Chem. Brit.* **1986**, *22*, 1001-1004.

[7] Johnstone T. C., Suntharalingam K., Lippard S. J., *Chem. Rev.* **2016**, *116*, 3436-3486.

[8] Hurley L. H., *Nat. Rev. Cancer* **2002**, *2*, 188-200.

[9] Jamieson E. R., Lippard S. J., *Chem. Rev.* **1999**, *99*, 2467-2498.

[10] Bruijnincx P. C. A., Sadler P. J., *Curr. Opin. Chem. Biol.* **2008**, *12*, 197-206.

[11] Waring M. J. *DNA-targeting Molecules as Therapeutic Agents*. RSC Publishing, **2018**.

[12] Cuello-Garibo J.-A., James C. C., Siegler M. A., Bonnet S., *Chem. Sq.* **2017**, *1*, 2.

[13] Saborit J. M., Caubet A., Brissos R. F., Korrodi-Gregorio L., Perez-Tomas R., Martinez M., Gamez P., *Dalton Trans.* **2017**, *46*, 11214-11222.

[14] Xu H., Morrical S. W. *Protein Motifs for DNA Binding*. John Wiley & Sons, Ltd, **2010**.

[15] Hannon M. J., *Chem. Soc. Rev.* **2007**, *36*, 280-295.

[16] Hannon M. J., Moreno V., Prieto M. J., Moldrheim E., Sletten E., Meistermann I., Isaac C. J., Sanders K. J., Rodger A., *Angew. Chem-Int. Edit.* **2001**, *40*, 880-884.

[17] Meistermann I., Moreno V., Prieto M. J., Moldrheim E., Sletten E., Khalid S., Rodger P. M., Peberdy J. C., Isaac C. J., Rodger A., Hannon M. J., *Proc. Natl. Acad. Sci. U. S. A.* **2002**, *99*, 5069-5074.

[18] Moldrheim E., Hannon M. J., Meistermann I., Rodger A., Sletten E., *J. Biol. Inorg. Chem.* **2002**, *7*, 770-780.

[19] Parajo Y., Malina J., Meistermann I., Clarkson G. J., Pascu M., Rodger A., Hannon M. J., Lincoln P., *Dalton Trans.* **2009**, 4868-4874.

[20] Hotze A. C. G., Hodges N. J., Hayden R. E., Sanchez-Cano C., Paines C., Male N., Tse M. K., Bunce C. M., Chipman J. K., Hannon M. J., *Chem. Biol.* **2008**, *15*, 1258-1267.

[21] Hamilton P. L., Arya D. P., *Nat. Prod. Rep.* **2012**, *29*, 134-143.

[22] Childs L. J., Malina J., Rolfsnes B. E., Pascu M., Prieto M. L., Broome M. L., Rodger P. M., Sletten E., Moreno V., Rodger A., Hannon M. J., *Chem-Eur. J.* **2006**, *12*, 4919-4927.

[23] Boer D. R., Kerckhoffs J., Parajo Y., Pascu M., Uson I., Lincoln P., Hannon M. J., Coll M., *Angew. Chem-Int. Edit.* **2010**, *49*, 2336-2339.

[24] Cardo L., Sadovnikova V., Phongtongpasuk S., Hodges N. J., Hannon M. J., *Chem. Commun.* **2011**, *47*, 6575-6577.

[25] Malina J., Hannon M. J., Brabec V., *Nucleic Acids Res.* **2008**, *36*, 3630-3638.

[26] Phongtongpasuk S., Paulus S., Schnabl J., Sigel R. K. O., Spingler B., Hannon M. J., Freisinger E., *Angew. Chem-Int. Edit.* **2013**, *52*, 11513-11516.

[27] Malina J., Hannon M. J., Brabec V., *Sci. Rep.* **2016**, *6*, 6.

[28] Casini A., Woods B., Wenzel M., *Inorg. Chem.* **2017**, *56*, 14715-14729.

[29] Zhao A. D., Howson S. E., Zhao C. Q., Ren J. S., Scott P., Wang C. Y., Qu X. G., *Nucleic Acids Res.* **2017**, *45*, 5026-5035.

[30] McNeill S. M., Preston D., Lewis J. E. M., Robert A., Knerr-Rupp K., Graham D. O., Wright J. R., Giles G. I., Crowley J. D., *Dalton Trans.* **2015**, *44*, 11129-11136.

[31] Malina J., Hannon M. J., Brabec V., *Febs J.* **2014**, *281*, 987-997.

[32] Brabec V., Howson S. E., Kaner R. A., Lord R. M., Malina J., Phillips R. M., Abdallah Q. M. A., McGowan P. C., Rodger A., Scott P., *Chem. Sci.* **2013**, *4*, 4407-4416.

[33] Aromi G., Gamez P., Reedijk J., *Coord. Chem. Rev.* **2008**, *252*, 964-989.

[34] Darawsheh M., Barrios L. A., Roubeau O., Teat S. J., Aromi G., *Chem-Eur. J.* **2016**, *22*, 8635-8645.

[35] Matsushita M. M., Yasuda T., Kawano R., Kawai T., Iyoda T., *Chem. Lett.* **2000**, 812-813.

[36] Baker T. M., Howard K. M., Brennessel W. W., Neidig M. L., *Acta Crystallogr. Sect. E-Crystallogr. Commun.* **2015**, *71*, m228-m229.

[37] Reichmann M. E., Rice S. A., Thomas C. A., Doty P., *J. Am. Chem. Soc.* **1954**, *76*, 3047-3053.

[38] Ghosh K., Kumar P., Tyagi N., Singh U. P., Aggarwal V., Baratto M. C., *Eur. J. Med. Chem.* **2010**, *45*, 3770-3779.

[39] Mandegani Z., Asadi Z., Asadi M., Karbalaei-Heidari H. R., Rastegari B., *Dalton Trans.* **2016**, *45*, 6592-6611.

[40] Kwak M. I., Jeon B. R., Kim S. K., Jang Y. J., *ACS Omega* **2018**, *3*, 946-953.

[41] Meyer-Almes F. J., Porschke D., *Biochemistry* **1993**, *32*, 4246-4253.

[42] Lakowicz J. R., Weber G., *Biochemistry* **1973**, *12*, 4161-4170.

[43] Berg J. M., Tymoczko J. L., Stryer L. Chapter 13: Membrane Channels and Pumps. *Biochemistry*, 5 edn. Freeman W. H. and Company, **2002**.

[44] Chen L. J., Yang H. B., Shionoya M., *Chem. Soc. Rev.* **2017**, *46*, 2555-2576.

[45] Chen T., Stephens P. A., Middleton F. K., Curtin N. J., *Drug Discov. Today* **2012**, *17*, 194-202.

[46] Vellas S. K., Lewis J. E. M., Shankar M., Sagatova A., Tyndall J. D. A., Monk B. C., Fitchett C. M., Hanton L. R., Crowley J. D., *Molecules* **2013**, *18*, 6383-6407.

[47] Sheldrick G. M. CELL_NOW, SAINT and TWINABS. Madison, Wisconsin, USA: Bruker AXS.

[48] Krause L., Herbst-Irmer R., Sheldrick G. M., Stalke D., *J. Appl. Cryst.* **2015**, *48*, 3-10.

[49] Sheldrick G. M., *Acta Crystallogr. Sect. C* **2015**, *71*, 3-8.

Received: 02 May 2018
Accepted: 07 November 2018
Published online: 20 November 2018

ORCID ID for authors
Luís Korrodi-Gregório: 0000-0002-2811-8081
Ricardo Pérez-Tomás: 0000-0003-3226-1240
Olivier Roubeau: 0000-0003-2095-5843
Patrick Gamez: 0000-0003-2602-9525